OPEN

Tuning the entanglement between orbital reconstruction and charge transfer at a film surface

B. Cui, C. Song, F. Li, G. Y. Wang, H. J. Mao, J. J. Peng, F. Zeng & F. Pan

Key Laboratory of Advanced Materials (MOE), School of Materials Science and Engineering, Tsinghua University, Beijing 100084, China.

The interplay between orbital, charge, spin, and lattice degrees of freedom is at the core of correlated oxides. This is extensively studied at the interface of heterostructures constituted of two-layer or multilayer oxide films. Here, we demonstrate the interactions between orbital reconstruction and charge transfer in the surface regime of ultrathin (La,Sr)MnO₃, which is a model system of correlated oxides. The interactions are manipulated in a quantitative manner by surface symmetry-breaking and epitaxial strain, both tensile and compressive. The established charge transfer, accompanied by the formation of oxygen vacancies, provides a conceptually novel vision for the long-term problem of manganites—the severe surface/interface magnetization and conductivity deterioration. The oxygen vacancies are then purposefully tuned by cooling oxygen pressure, markedly improving the performances of differently strained films. Our findings offer a broad opportunity to tailor and benefit from the entanglements between orbit, charge, spin, and lattice at the surface of oxide films.

Semiconductor heterostructures have brought about prominent advances in a variety of mainstream electronics over the last few decades[1,2]. Efforts are increasingly shifting to artificially constructed oxide heterostructures, generating a rich spectrum of exotic properties and unexpected states at the interface[3–10]. For example, the emergence of high-mobility conductivity and interfacial magnetism at the classic $LaAlO_3/SrTiO_3$ interface bridges the freedom of charge, spin, and lattice because of the $(TiO_2)-(LaO)^+$ sequence[3–6]. Interfacial orbital reconstruction has led to exchange bias and covalent bonding in $(La,Sr)MnO_3/BiFeO_3$ and $(La,Sr)MnO_3/$ cuprate systems, reflecting the coupling between orbital and spin/charge, respectively[7,8]. The surface, which plays a critical role in the integration of an oxide film into electronic devices, experiencing both lattice and orbital reconstruction due to the lattice symmetry-breaking in the free surface, has stimulated extensive research and development[11,12]. However, the interplay between the four degrees of freedom in this regime, especially orbital reconstruction and charge transfer, has thus far remained a question of interest lacking experimental insight.

In this work, we combine the results of x-ray absorption spectroscopy (XAS) and x-ray linear dichroism (XLD), which measure the electronic structure and orbital occupancy[9], with magnetization, transport, and calculations to quantitatively investigate the interplay between orbital reconstruction and charge transfer in $(La,Sr)MnO_3$ (LSMO). LSMO has been selected as a model system for both magnetic materials and correlated oxides, providing a unique arena for creating the coupling of several degrees of freedom in a single oxide film[13,14]. Additionally, mixed-valence LSMO with half-filled e_g orbits of Mn^{3+} guarantees the sensitivity of its magnetic and electric properties to lattice distortion and orbital ordering by strain engineering[15–18]. Finally, note that the electrostatic potential between $(La_{2/3}Sr_{1/3}O)^{2/3+}$ and $(MnO_2)^{2/3-}$ drives charge transfer between these two sublayers, similar to polarity discontinuities at the $LaAlO_3/SrTiO_3$ interface[19]. In addition to its fundamental significance, we also use the couplings in the surface regime to revisit the notorious behavior in ultrathin LSMO films—the loss of magnetization and metallic conductivity. With this compass, the performances of manganite films are greatly improved.

Results

Strain dependent Mn valence state. $La_{2/3}Sr_{1/3}MnO_3$ (001) (LSMO) films ranging from 5 unit cells (u.c.) to 125 u.c. under tensile to compressive strain states are obtained by growth on different substrates. MgO, $Pb(Mg_{1/3}Nb_{2/3})_{0.72}Ti_{0.28}O_3$ (PMN-PT), and $SrTiO_3$ (STO) are substrates used for tensile strain, while $LaAlO_3$ (LAO) and $LaSrAlO_4$ (LSAO) are used for compressive strain and result in the following strain values: $\varepsilon_0 = 8.9\%$,

4.0%, 0.9%, −2.1%, and −2.9% (see Supplementary Figs. S1 and S2). The existence of strain suppresses the magnetization and metallic conductivity of ultrathin LSMO films[17,20]. It is mainly because that the enhancement of tensile (compressive) strain enlarges the lattice in the a–b plane (c-axis), which stabilizes the A-type (C-type) antiferromagnetic phases in the film and destroys the double exchange (DE) effect[15–17]. This is indeed observed in our ultrathin samples with thicknesses of 5 and 15 u.c., although the Curie temperatures (T_C) recover close to the bulk value, along with the metallic conductivity, as the thickness of LSMO increases to 125 u.c. Therefore, regardless of the sign of strain, strain engineering plays a trivial role in the performances of samples that far exceed the critical thickness (see Supplementary Fig. S3).

To investigate the strain effect on the charge degree of freedom of LSMO films, XAS carried out in total electron yield (TEY) mode, which is an extremely sensitive probe for electronic structure, is performed to study the manganese valence of LSMO films grown on different substrates. The polarization directions of the linearly polarized x-rays are tuned by rotating the x-ray incident angle, with 90° and 30° incident corresponding to in-plane (E//a) and out-of-plane (E//c) polarization components, respectively, as shown in Fig. 1a. The XAS in Fig. 1b and c show the in-plane component. The out-of-plane components exhibit the same peak positions and are used to acquire XLD data, as explained in the following analysis. The most eminent features in Fig. 1b occur for the peaks of Mn-L_3 in 15 u.c. samples, for which gradually shifts towards lower energies are present in decreasing order for MgO, PMN-PT, STO, LAO and LSAO with amplitudes of ~0.6 eV. These shifts suggest that the Mn valence decreases in this series. Comparisons of XAS spectra for reference materials containing Mn^{3+} and Mn^{4+} ions yield absorption peak values for Mn^{3+} 1.5 eV lower than that of Mn^{4+}, allowing a rough estimate of $0.4e^-$ difference per manganese ion in MgO and LSAO substrates[21], where e^- is the charge on the electron. Because the signal of XAS in TEY mode reflects the valence state of surface Mn ions[8,17], these results substantiate that the strain in thin LSMO films (e.g., 15 u.c.) strongly affects the surface region. Conversely, the valences of Mn ions are identical between the 125 u.c. LSMO films with strain relaxation on different substrates (Fig. 1c), which further supports the importance of strain induced by film/substrate mismatch in the electronic structure of film surface. We therefore conclude that strain is an effective way to tailor the Mn valence of manganite.
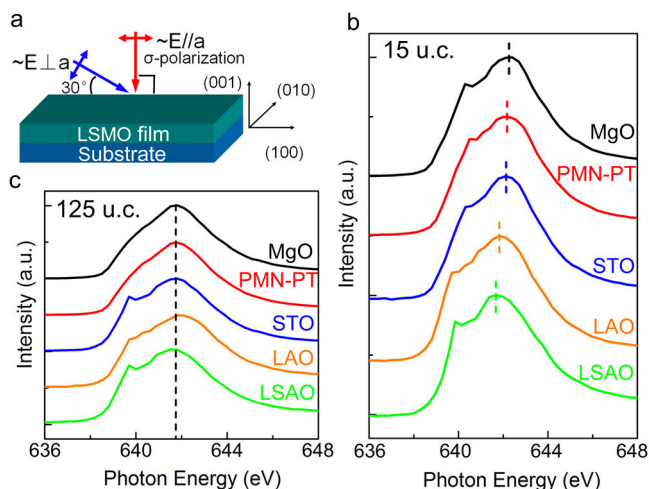

Figure 1 | Shift of Mn L_3 edge peak position. (a), Schematic of experimental configuration for XAS measurements with different x-ray incident angles. (b) and (c), Normalized XAS (in-plane) at Mn-L_3 absorption edge for 15 u.c. and 125 u.c. LSMO grown on different substrates, respectively.

The effects of strain and surface symmetry-breaking on orbital reconstruction. To elucidate charge redistribution in LSMO, we investigate the orbital occupancy of manganites on different substrates firstly. Representative XAS and XLD results, where XLD is the difference between the XAS in-plane and out-of-plane components, $I_{ab} − I_c$, of LSMO on MgO and LAO substrates, are presented in Fig. 2a–f, giving information for the occupancy of Mn-$3d$ orbits. The XAS with two incident angles are normalized according to the L_3 peak and the area under XLD around the L_2 peak (647.5 eV–660.0 eV) (A_{XLD}) is used to represent the difference between the relative occupancies of the $3z^2 − r^2$ and $x^2 − y^2$ orbits [$A_{XLD} = P(3z^2 − r^2) − P(x^2 − y^2)$] (Ref.12). The XLD signal around the L_2 peak derived from the normalized XAS spectra is negative for the films on MgO, indicating enhanced $x^2 − y^2$ electron occupancy for films strained under tension (Fig. 2a–c). In contrast, compressive strain stabilizes the $3z^2 − r^2$ orbit, resulting in positively valued XLD signals for the LSMO on LAO (Fig. 2d–f). The effect of strain on orbital reconstruction is further confirmed in LSMO on PMN-PT, STO, and LSAO substrates (see Supplementary Fig. S4).

The relationship of film thickness and A_{XLD} for the LSMO films on all substrates is displayed in Fig. 2g (symbols, left axis). Notably, A_{XLD} for 5 u.c. LSMO on PMN-PT and STO is unexpectedly positive, substantiating that strain is not the sole driving force for orbital occupancy in these ultrathin films. The origin of this anomalously positive signal is the surface symmetry-breaking attributed to the absence of apical oxygen coordination[12,22,23], which brings about an additional out-of-plane occupancy and counterbalances the tensile strain favored in-plane orbits[22]. Given that the contributions of n MnO_2 slabs depend on both their positions with respect to the surface and the attenuation depth (δ), the intensity of the XLD signal can be fitted as follows[12]

$$A_{XLD} \sim I_{XLD\_norm} = \frac{\sum_{i=1}^{n} [P_{t_i}(3z^2 − r^2) − P_{t_i}(x^2 − y^2)]\cdot \exp(−t_i/\delta)}{\sum_{i=1}^{n} \exp(−t_i/\delta)} \quad (1)$$

where $P_{t_i}(3z^2 − r^2)$ and $P_{t_i}(x^2 − y^2)$ are the relative occupancies of the $3z^2 − r^2$ and $x^2 − y^2$ orbits, respectively, for the MnO_2 slab at a distance t_i from the free surface. For the fully strained films (see Supplementary Fig. S2), the XLD signal of Eq. (1) can be calculated by three parameters: the occupation of the surface, $P_S = P_S(3z^2 − r^2) − P_S(x^2 − y^2)$, the occupation of the bulk, $P_b = P_b(3z^2 − r^2) − P_b(x^2 − y^2)$, and the attenuation depth δ (see Supplementary Fig. S5). For thicknesses less than 30 u.c., curves fitted using the experimental data are shown by the dashed lines in Fig. 2g (dashed lines, right axis), and the corresponding P_S and P_b are summarized in Table 1. The attenuation depth (δ) approximately equals to 4.6 nm, in agreement with previous works[8,17].

Notably, experimental points are well fitted under 30 u.c., whereas for thicker films, considerable strain relaxation weakens the orbital reconstruction, leading to experimental values with A_{XLD} far above (below) fitted curves for tensile (compressive) strain. These discrepancies may be attributed to the critical thickness for strain relaxation (see Supplementary Fig. S2). The bulk component is dependent on the strain: P_b increases from negative to positive sequentially for MgO, PMN-PT, STO, LAO and LSAO, as listed in Table 1. In contrast, the surface electron occupancy, P_S, is found to always be preferred at the $3z^2 − r^2$ orbit, irrespective of the sign of the strain in the films due to surface symmetry-breaking. The resultant large splitting between the e_g orbits at the surface and the corresponding orbital reconstruction gives rise to charge transfer and Mn valence variation for the different substrates, which will be discussed below.

Charge transfer and the formation of oxygen vacancies. As the orbital and electronic structure of LSMO under the influence of
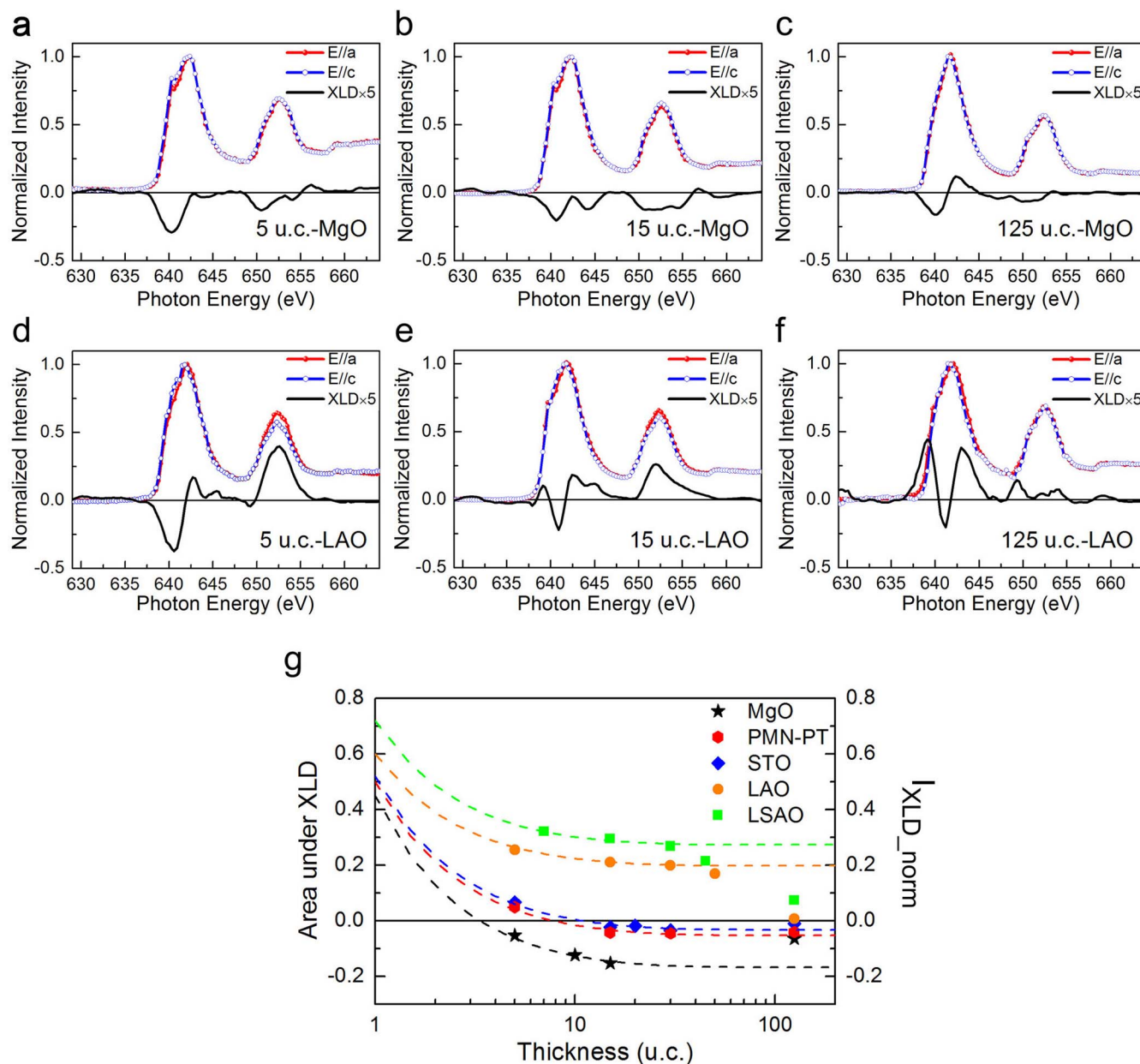
Figure 2 | X-ray linear dichroism and XLD signal versus sample thickness. (a–c) and (d–f), Normalized XAS and XLD of LSMO with different thicknesses of 5 u.c., 15 u.c. and 125 u.c. grown on MgO and LAO substrates, respectively. (g), Left axis (symbols): integrated area of the XLD signal of the samples grown on different substrates. Right axis (dashed lines): best fits of area under XLD signal to Eq. (1) as explained in the text.

strain and surface symmetry-breaking is clarified, we develop an electrostatic model in Fig. 3 to describe the charge transfer in the films. In the absence of strain and surface effects, each Mn e_g orbit obtains $1/3 e^-$ from the adjacent $La_{2/3}Sr_{1/3}O$ layer ($1/6 e^-$ for the surface Mn e_g orbit), as shown in Fig. 4a. Although the crystalline quality of the LSMO films grown on other substrates are not as good as that on STO, they are quasi-epitaxial without any phase and composition separation at a thickness of 15 u.c.[9]. It is also noteworthy that the influence of the lattice distortion due to the film/substrate mismatch on the charge transfer has been taken into account in the orbital reconstruction in our model. The splitting of e_g orbits leads to the rearrangement of uniformly distributed electrons within or between the layers. For the bulk part of LSMO films, the orbital occupancies are changed according to P_b (Table 1) without external charge transfer and valence variation. For the surface layer, $3z^2 - r^2$ orbital energy levels are much lower than that of bulk ones[23];

hence, electrons at the second MnO_2 layer ($i = 2$) are transferred to the surface energetically favorable $3z^2 - r^2$ orbit through the out-of-plane Mn-O-Mn covalent bonds. These bonds are hybridized by the O-$2p$ orbit and two adjacent Mn $3z^2 - r^2$ orbits and serve as a preferential high-mobility passageway for electron transfer due to their highly overlapped electron cloud[16], as displayed in Fig. 4b. With fixed $1/6$ electrons at the surface $x^2 - y^2$ orbits, the maximum transfer of electrons between MnO_2 (from the $i = 2$ to $i = 1$) layers (n_1) via (La,Sr)O is $2/3$, which generates an extreme orbital component described by $\frac{P_S(3z^2 - r^2)}{P_S(x^2 - y^2)} = 5$ and an ionic Mn^{3+} state at the surface. However, for larger out-of-plane orbital components, the transfer of electrons from the surface $x^2 - y^2$ to $3z^2 - r^2$ (n_2) is allowed, and the effects should be considered. Given that the orbital component $\frac{P_S(3z^2 - r^2)}{P_S(x^2 - y^2)}$ shown in Table 1 determines the

Table 1 | Calculated results of the orbital occupation, charge transfer, electric potential offset, and oxygen vacancy concentration

Substrate	P_S	P_b	$\dfrac{P_S(3z^2-r^2)}{P_S(x^2-y^2)}$	n_1	n_2	m	V/eV	x
MgO	0.450	−0.220	2.636	$0.273e^-$	0.000	3.394	0.273	0.019
PMN-PT	0.500	−0.100	3.000	$0.333e^-$	0.000	3.333	0.333	0.024
STO	0.520	−0.080	3.167	$0.361e^-$	0.000	3.306	0.361	0.026
LAO	0.600	0.160	4.000	$0.500e^-$	0.000	3.167	0.500	0.036
LSAO	0.720	0.230	6.143	$0.667e^-$	$0.027e^-$	3.000	0.667	0.048

surface charge redistribution, the relationship between the number of transferred electrons and orbital components can be expressed by

$$\frac{n_1+n_2+\frac{1}{6}}{\frac{1}{6}-n_2}=\frac{P_S(3z^2-r^2)}{P_S(x^2-y^2)} \qquad (2)$$

From Eq. (2), we can derive the following equations to calculate the transferred electrons between the layers n_1 and the orbits in the surface layer n_2,

$$n_1=\begin{cases}\frac{1}{6}\left(\frac{P_S(3z^2-r^2)}{P_S(x^2-y^2)}-1\right) & \frac{P_S(3z^2-r^2)}{P_S(x^2-y^2)}\leq 5 \\ \frac{2}{3} & \frac{P_S(3z^2-r^2)}{P_S(x^2-y^2)}>5\end{cases} \qquad (3)$$

$$n_2=\begin{cases}0 & \frac{P_S(3z^2-r^2)}{P_S(x^2-y^2)}\leq 5 \\ \frac{1}{6}-1\Big/\left(\frac{P_S(3z^2-r^2)}{P_S(x^2-y^2)}+1\right) & \frac{P_S(3z^2-r^2)}{P_S(x^2-y^2)}>5\end{cases} \qquad (4)$$

The values of n_1 and n_2 for various substrates calculated by Eqs. (3) and (4) are also listed in Table 1. The valence state of Mn (m) at the surface is determined by the interlayer charge transfer, $m=3\frac{2}{3}-n_1$. Consequently, the estimated valence states of Mn are 3.394, 3.333, 3.306, 3.167 and 3.000 for LSMO grown on MgO, PMN-PT, STO, LAO and LSAO substrates, respectively, in accordance with the shift of the Mn-L_3 peak in Fig. 1b. Similarly, the charge transfer difference ($\Delta n_1 = 0.394e^-$) between MgO and LSAO substrates exactly coincides with the charge variation of the Mn ions ($0.4e^-$) mentioned above. It is therefore concluded that the coherence of the valence state characterization and the electrostatic model with respect to XLD results provides compelling evidence for the coupling between orbital reconstruction and charge transfer.

The polar discontinuities play a dominant role in the charge transfer at the film/substrate interface, as seen in LaAlO$_3$/SrTiO$_3$. The effect of such charge transfer commonly affects the valence state of the constituent in the vicinity of the interface, for example, Ti^{4+} → Ti$^{3.5+}$ in SrTiO$_3$ close to the LaAlO$_3$/SrTiO$_3$ interface. Because the interfacial effect near the surface is quite weak, it is highly unlikely—although not impossible—that charge transfer originates primarily from charge redistribution in this region. Instead, the charge transfer in 15 u.c. LSMO is more feasibly motivated by orbital reconstruction. In addition, the present charge transfer model for the 15 u.c. thick sample is based on orbital reconstruction, which is detected by XLD measurements in TEY mode with an attenuation depth of ~4 nm, outside of the scope of the interfacial regime. As the LSMO film thickness is reduced to 5 u.c., the Mn-L_3 peaks shift toward a lower energy in sequential order for MgO, PMN-PT, and STO substrates with decreasing tensile stress, similar to the 15 u.c. samples. Nevertheless, the possibility of electronic phase separation and polar discontinuities might complicate Mn valence investigations for several monolayer thick LSMO grown on LAO (see Supplementary Fig. S6).

The surface charge redistribution results in an electric potential offset (V) with an amplitude proportional to the amount of transferred charge. The potential before (black dashed lines) and after (red lines) surface charge redistribution can be clearly delineated in the electric potential diagrams in Fig. 3a and b. Specifically, n_1 is equally constituted by electrons from two (La,Sr)O layers adjacent to a MnO$_2$ layer ($i = 2$), while $n_1/2$ electrons from the (La,Sr)O layer nearest to the surface contribute to the electric potential of surface MnO$_2$ ($i = 1$). Hereby, after the surface charge redistribution, the electric potential of the (La,Sr)O layer nearest to the surface is ($n_1/2–1/6$) eV, while the potential difference between the surface MnO$_2$ and its adjacent (La,Sr)O layer is ($1/3 + n_1/2$) eV. This sum is the absolute electric potential of the surface MnO$_2$ layer, in contrast to the 1/6 eV before redistribution, described by

$$V=\frac{1}{3}+\frac{n_1}{2}+\left(\frac{n_1}{2}-\frac{1}{6}\right)-\frac{1}{6}=n_1 \qquad (5)$$

Corresponding results for potential offsets can be found in Table 1 for various substrates. We note that the internal charge redistribution in the LSMO film maintains the same electric potential between the substrate and surface. The ordered oxygen vacancy (V_O) in alternate MnO$_{2-x}$ layers allow more electrons in the (La,Sr)O layer to be transferred to the stoichiometric MnO$_2$ layers as the Mn valence should be uniform in the bulk films[24,25], providing an effective avenue for the elimination of potential offset. Such charge redistribution reduces the Mn valence in both MnO$_2$ and MnO$_{2-x}$ layers, as shown in the bottom of Fig. 3c and d (blue arrows and potential lines). For films strained under tension, the oxygen deficiencies are less and the Mn valence is comparatively higher with a smaller offset, while the compressive ones possess more V_O and lower Mn valence. Quantitatively, each MnO$_{2-x}$-(La,Sr)O-MnO$_2$ unit reduces the electrical potential by $2x$ eV. V_O in bulk MnO$_{2-x}$ layers (x) is determined in the film with a thickness of 15 u.c., $x = V/14 = n_1/14$ (the bulk includes 14 layers in the 15 u.c. sample), producing values of $x = 0.019, 0.024, 0.026, 0.036,$ and 0.048 for MgO, PMN-PT, STO, LAO and LSAO substrates, respectively (Table 1). The formation of additional V_O weakens the double exchange in the reconstructed surface and results in an antiferromagnetic phase, leading to the loss of ferromagnetism and metallic conductivity at the surface or, when ultrathin, in the entire film. It is noteworthy that the charge transfer in our case is in a single LSMO film rather than in heterostructures such as LaAlO$_3$/SrTiO$_3$ (Ref. 19). However, strain relaxation would weaken the difference in surface orbital reconstruction (Fig. 2g), thus suppressing the charge transfer between MnO$_2$ slabs and the concomitant Mn valence variation in the 125 u.c. samples. Hence, the results in Fig. 1c are well supported. We therefore summarize that charge redistribution is driven by the orbital reconstruction through the orbital component $\dfrac{P_S(3z^2-r^2)}{P_S(x^2-y^2)}$ in 15 u.c. thick LSMO with different strain states, reaching a consistent charge transfer value with the Mn valence variation in XAS.

Oxygen vacancy manipulation for high performance of manganite. Thus far, the electrostatic model has described both the charge redistribution and the introduction of V_O in the charge deviation of Mn valence from its ideal value, which serves as the intrinsic origin of
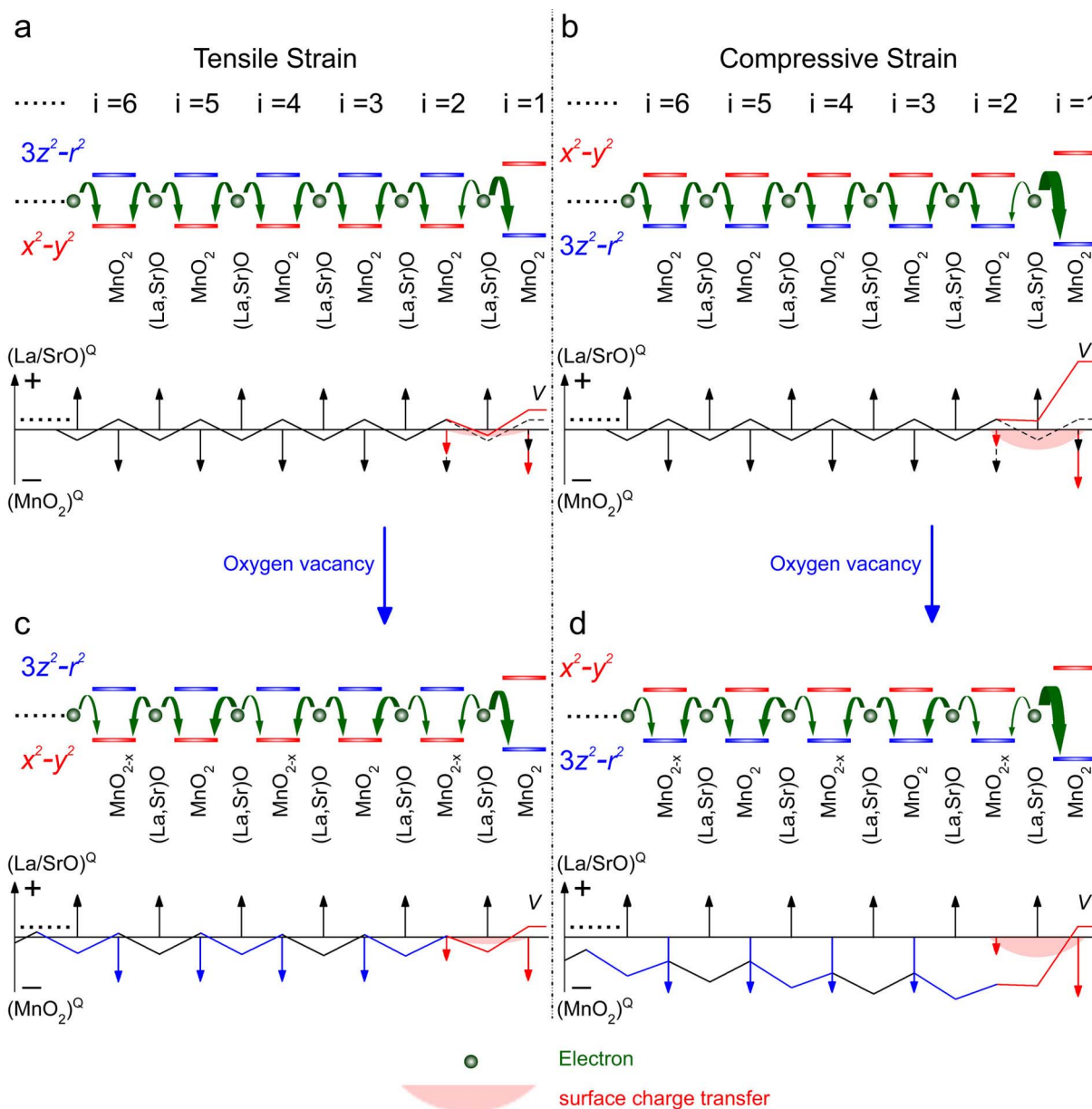
Figure 3 | Schematic illustration of charge redistribution and oxygen vacancy formation in LSMO film near surface region. The e_g energy level splitting, charge redistribution (top) and corresponding electric potential (bottom) schematic for LSMO films near the surface region without (a and b) or with (c and d) regard to the formation of oxygen vacancies. The green arrows mark the electrons transferred from (La,Sr)O layers to MnO_2 slabs. The wider the arrow is, the more electrons are transferred. The arrows in electric potential schematic are the charges of (La,Sr)O and MnO_2 layers. The charge and potential variation induced by surface charge redistribution and oxygen vacancies are highlighted in red and blue, respectively.

the severe deterioration of surface ferromagnetism and conductivity. It has been demonstrated previously that several methods, such as electrostatic doping[26] and ferroelectric polarization[27], provide an opportunity to the tune electronic and magnetic properties of manganite through the manipulation of carrier concentration. We now address V_O manipulation and its effect on performance enhancement in LSMO. Because the electric potential offset is sensitive to oxygen deficiencies (MnO_5) at the surface, the oxygen pressure used in the sample cooling process is expected to effectively control both the potential offset and V_O. Consequently, samples of 15 u.c. on various substrates with different cooling oxygen pressures, $p_C = 50$, 300 and 550 Torr, are prepared, in which 300 Torr was employed for the samples discussed above. Concomitant O-K edge XAS of LSMO on MgO, STO and LAO substrates cooled under different oxygen pressures are normalized according to the feature

peak of the Mn-$3d$ orbit at approximately 530 eV and shown in Fig. 5. The pre-edge spectral region extending from 529 to 533 eV represents the Mn $3d$ unoccupied states and the second band of Mn $3d$ at approximately 533 eV (marked by the dashed line) is quite sensitive to the valence of Mn[28,29]. Compared with the LSMO on STO and LAO, the second band of Mn $3d$ is much more prominent for films on MgO with a higher Mn valence. On the other hand, as p_C increases, the peaks at approximately 533 eV are apparently enhanced regardless of the substrate, indicating the reduction of V_O and Mn^{3+} (which can be found in the magnified view in Supplementary Fig. S7).

As a typical sample showing tensile strain (Fig. 3c), LSMO on MgO substrate with less intrinsic V_O exhibits a higher T_C and lower resistivity under a lower cooling oxygen pressure ($p_C = 50$ Torr), which causes more V_O (Fig. 6a and d). Similar to the samples with the MgO
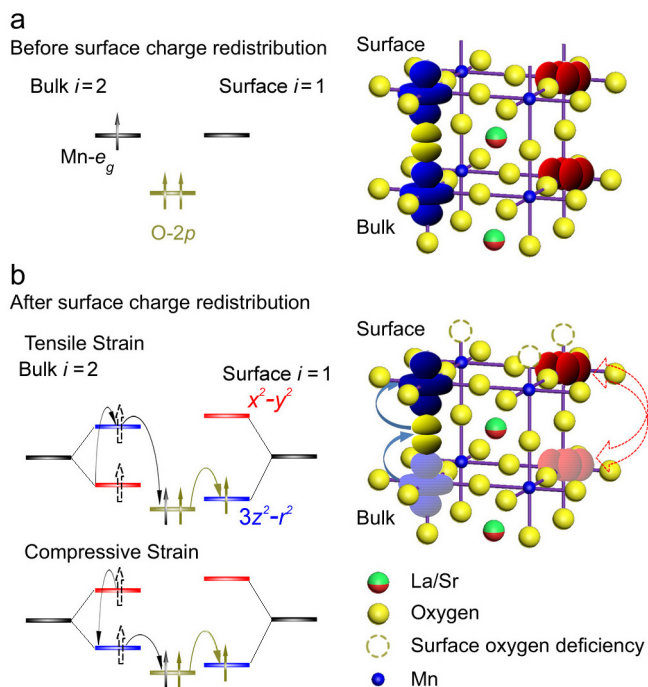
Figure 4 | Schematic of charge transfer through Mn-O-Mn covalent bond. (a), Sketch for the charge distribution (left column) and orbit information (right column) of Mn e_g and O $2p$ orbits near the surface without consideration of strain and surface symmetry-breaking effect. (b), The charge transfer schematic from bulk to surface for the films under tensile or compressive strain (left column) and corresponding high-mobility charge transfer passageway formed by two $3z^2 - r^2$ orbits and O $2p$ orbit (right column). The electron at bulk orbits ($x^2 - y^2$ or $3z^2 - r^2$) are transferred to the surface $3z^2 - r^2$ orbit through the out-of-plane Mn-O-Mn covalent bond as the arrows shown, leaving less filled orbits (washy in the schematic) in the bulk.

substrate, a reduced V_O has a negative effect on the magnetic and electric properties of films grown on STO (Fig. 6b and e). However, when the oxygen cooling experiments are performed on the samples with compressive strain, the situation changes dramatically. The films with compressive strain grown on LAO exhibit semiconducting behavior because the resistance is seen to increase with decreasing temperature, in analogy to the case on MgO and STO, when $p_C = 50$ and 300 Torr. As the cooling oxygen pressure increases to 550 Torr, it is surprisingly found that the films on LAO show a typical character of metallic conductivity (Fig. 6f). This behavior is opposite to that of the films under tensile strain. Generally, high oxygen pressure

annealing would lead to a resistance increase. In the present case, however, the transition from semiconducting to metallic conductivity with increasing oxygen pressure confirms that oxygen compensates for the V_O induced by the elimination of the potential offset. This process strengthens the double-exchange effect in LSMO. Accordingly, the films exhibit robust magnetization, and the T_C of LSMO is greatly enhanced from $\sim$200 K to 250 K by increasing p_C from 50 to 550 Torr, as shown in Fig. 6c. The results from the effective manipulation of the magnetization and conductivity of LSMO by tensile and compressive strains indicating that our electrostatic model for the both charge redistribution and V_O is confirmed by an elegant experimental design, shedding promising light on the development of manganite-based spintronics.

Discussion

The present results verify the existence of interactions between orbit (orbital reconstruction), charge (charge transfer), lattice (epitaxial strain), and spin (magnetization) in the surface regime of a single LSMO film. Surface symmetry-breaking and strain, as well as changing the orbital energy levels and occupancies of Mn ions, lead to charge redistribution throughout the films. The quantitative dependence of charge transfer on orbital reconstruction $\left(\frac{P_S(3z^2 - r^2)}{P_S(x^2 - y^2)}\right)$ established in an electrostatic model sheds promising light on the preparation of a single oxide film where the four degrees of freedom act on each other, including but not limited to the manganite perovskite we have presented here. The understanding of the interactions at the film surface serves as the compass to improve the performance at the surface or throughout ultrathin LSMO films. The charge redistribution associated with the introduction of V_O to modify the potential offset, which depends on the strain state, is then verified to be tunable by a facile, reliable, and efficient design—the oxygen pressure control in the cooling process, leading to an enhancement of the magnetization and conductivity at a lower (higher) oxygen pressure for the tensile (compressive) case. Thus, this aspect would optimize the interface between manganite/non-magnetic materials (such as LSMO/SrTiO₃ in magnetic tunnel junctions and LSMO/graphene in spin injection devices) that ultimately restricted the performances of oxide spintronics. At last, we note that the improvements introduced in this work can be readily generalized to other oxide films, and thus has the potential to generate a variety of unprecedented properties at film surface.

Methods

Sample preparation. All of the samples were grown using pulsed laser deposition (PLD) from a stoichiometric La₂/₃Sr₁/₃MnO₃ target by applying a KrF excimer laser at a rate of 1.16 nm/min. During growth, the substrate was held at 700°C and in an oxygen background pressure of 200 mTorr. The growth was monitored in situ by RHEED (reflection high-energy electron diffraction) analysis allowing precise control of the
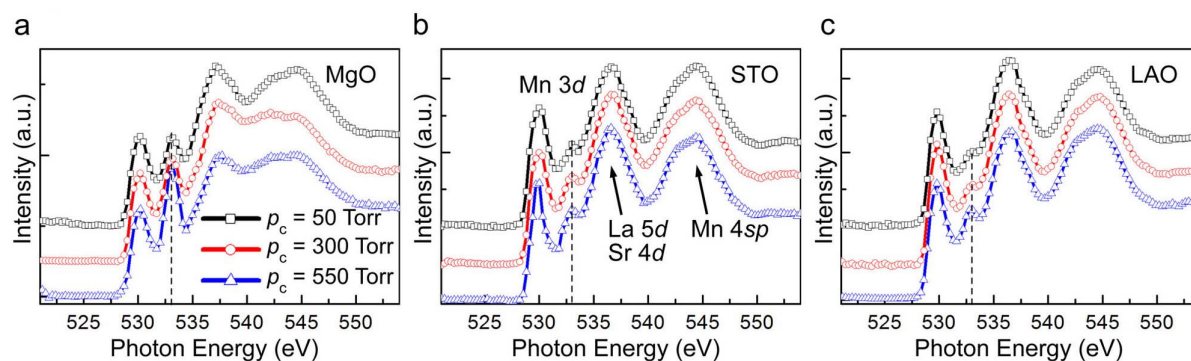

Figure 5 | O-K edge of LSMO under different cooling pressure. (a–c), O-K edge of 15 u.c. LSMO cooled in different oxygen pressures ($p_C = 50$, 300 and 550 Torr) grown on representative substrates, MgO, STO and LAO, respectively. The dashed lines mark the Mn $3d$ relevant absorption peak around 533 eV. The peaks marked by arrows at 536 eV and 545 eV are assigned to the bands with La $5d$/Sr $4d$ and Mn $4sp$ character, respectively.
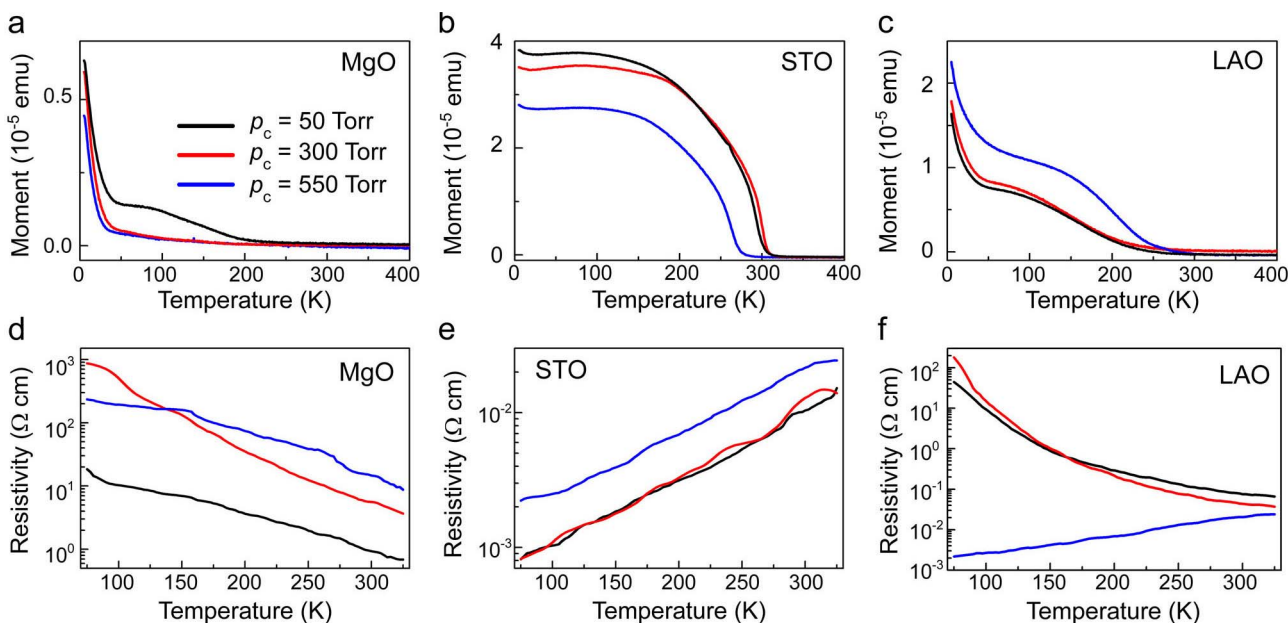
Figure 6 | Magnetization and conductivity of LSMO films cooled under various oxygen pressures. (a–c), Magnetization versus temperature curves for 15 u.c. LSMO cooled in different oxygen pressures (p_C = 50, 300, and 550 Torr) grown on representative substrates, MgO, STO and LAO, respectively. Corresponding resistivities as a function of temperature are shown in (d–f).

thickness at the unit cell scale and accurate characterization of the growth dynamics. Without special instruction, the samples were slowly cooled to room temperature in 300 Torr of oxygen at a rate of ~5°C/min to improve the oxidation level after growth.

Sample characterization. A Quantum Design superconducting quantum interference device (SQUID) measurement system (QD MPMS-7) was used to measure the magnetic properties along the (100) direction of the substrate in the temperature range 5–400 K, which could detect the slight variation of magnetization with a resolution of 10^{-7} emu[30]. All the field-cooling M–T (magnetization versus temperature) measurements in this work were carried out without any magnetic field after cooling down to 5 K in 20 kOe. Conductivity was determined in a Van der Pauw four-probe configuration by the ET9000 electric transport measurement system. XAS measurements were performed in total electron yield (TEY) mode at the Beamline BL08U1A in Shanghai Synchrotron Radiation Facility. The polarization directions of the linearly polarized x-rays are tuned by rotating the x-ray incident angle, with 90° and 30° corresponding to in-plane (E//a, I_{ab}) and majority of out-of-plane (E//c, I_c), respectively. The spectra normalization was made by dividing the spectra by a factor such that the L_3 pre-edge and L_2 post-edge have identical intensities for the two polarizations. After that, the pre-edge spectral region was set to zero and the peak at the L_3 edge was set to one. X-ray linear dichroism (XLD), the difference between the two measurements (I_{ab}–I_c), gives direction insight of the empty Mn $3d$ states. The O-K edge XAS was measured with an incidence angle of 90°. The measurement temperature for XAS and XLD is 300 K.

1. Kroemer, H. Quasielectric fields and band offsets: teaching electrons new tricks. *Rev. Mod. Phys.* **73**, 783–793 (2001).
2. Chappert, C., Fert, A. & Nguyen van Dau, F. The emergence of spin electronics in data storage. *Nature Mater.* **6**, 813–823 (2007).
3. Hwang, H. Y. *et al.* Emergent phenomena at oxide interfaces. *Nature Mater.* **11**, 103–113 (2012).
4. Ohtomo, A. & Hwang, H. Y. A high-mobility electron gas at the LaAlO₃/SrTiO₃ heterointerface. *Nature* **427**, 423–426 (2004).
5. Reyren, N. *et al.* Superconducting interfaces between insulating oxides. *Science* **317**, 1196–1199 (2007).
6. Brinkman, A. *et al.* Magnetic effects at the interface between non-magnetic oxides. *Nature Mater.* **6**, 493–496 (2007).
7. Yu, P. *et al.* Interface control of bulk ferroelectric polarization. *Proc. Natl. Acad. Sci. USA* **109**, 9710–9715 (2012).
8. Chakhalian, J. *et al.* Orbital reconstruction and covalent bonding at an oxide interface. *Science* **318**, 1114–1117 (2007).
9. Cui, B. *et al.* Strain engineering induced interfacial self-assembly and intrinsic exchange bias in a manganite perovskite film. *Sci. Rep.* **3**, 2542; doi:10.1038/srep02542 (2013).
10. Ward, T. Z. *et al.* Tuning the metal-insulator transition in manganite films through surface exchange coupling with magnetic nanodots. *Phys. Rev. Lett.* **106**, 157207 (2011).
11. Zhu, G. Z., Radtke, G. & Botton, G. A. Bonding and structure of a reconstructed (001) surface of SrTiO₃ from TEM. *Nature* **490**, 384–387 (2012).
12. Pesquera, D. *et al.* Surface symmetry-breaking and strain effects on orbital occupancy in transition metal perovskite epitaxial films. *Nature Commun.* **3**, 1189 (2012).
13. Dagotto, E. Complexity in strongly correlated electronic systems. *Science* **309**, 257–262 (2005).
14. Coey, J. M. D., Viret, M. & von Molnár, S. Mixed-valence manganites. *Adv. Phys.* **48**, 167–293 (1999).
15. Tebano, A. *et al.* Evidence of orbital reconstruction at interfaces in ultrathin La₀.₆₇Sr₀.₃₃MnO₃ films. *Phys. Rev. Lett.* **100**, 137401 (2008).
16. Lepetit, M. B., Mercey, B. & Simon, C. Interface effects in perovskite thin films. *Phys. Rev. Lett.* **108**, 087202 (2012).
17. Lee, J. S. *et al.* Hidden magnetic configuration in epitaxial La₁₋ₓSrₓMnO₃ films. *Phys. Rev. Lett.* **105**, 257204 (2010).
18. May, S. J. *et al.* Enhanced ordering temperatures in antiferromagnetic manganite superlattices. *Nature Mater.* **8**, 892–897 (2009).
19. Nakagawa, N., Hwang, H. Y. & Muller, D. A. Why some interfaces cannot be sharp. *Nature Mater.* **5**, 204–209 (2006).
20. Mao, H. J. *et al.* Room temperature spontaneous exchange bias in (La,Sr)MnO₃/PbZr₀.₈Ti₀.₂O₃/(La,Sr)MnO₃ sandwich structure. *J. Appl. Phys.* **114**, 043904 (2013).
21. Horiba, K. *et al.* Electronic structure of SrRu₁₋ₓMnₓO₃ studied by photoemission and x-ray absorption spectroscopy. *Phys. Rev. B* **81**, 245127 (2010).
22. Aruta, C. *et al.* Orbital occupation, atomic moments, and magnetic ordering at interfaces of manganite thin films. *Phys. Rev. B* **80**, 014431 (2009).
23. Calderón, M. J., Brey, L. & Guinea, F. Surface electronic structure and magnetic properties of doped manganites. *Phys. Rev. B* **60**, 6698–6704 (1999).
24. Ferguson, J. D. *et al.* Epitaxial oxygen getter for a brownmillerite phase transformation in manganite films. *Adv. Mater.* **23**, 1226–1230 (2011).
25. Kim, Y. M. *et al.* Probing oxygen vacancy concentration and homogeneity in solid-oxide fuel-cell cathode materials on the subunit-cell level. *Nature Mater.* **11**, 888–894 (2012).
26. Ahn, C. H. *et al.* Electrostatic modification of novel materials. *Rev. Mod. Phys.* **78**, 1185–1212 (2006).
27. Dong, S. & Dagotto, E. Full control of magnetism in a manganite bilayer by ferroelectric polarization. *Phys. Rev. B* **88**, 140404(R) (2013).
28. Abbate, M. *et al.* Controlled-valence properties of La₁₋ₓSrₓFeO₃ and La₁₋ₓSrₓMnO₃ studied by soft-x-ray absorption spectroscopy. *Phys. Rev. B* **46**, 4511–4519 (1992).
29. Mannella, N. *et al.* Temperature-dependent x-ray absorption spectroscopy of colossal magnetoresistive perovskites. *Phys. Rev. B* **71**, 125117 (2005).
30. Chen, G. *et al.* Resistive Switching and Magnetic Modulation in Cobalt-Doped ZnO. *Adv. Mater.* **24**, 3515–3520 (2012).

Author contributions

Additional information